

The trans-lithospheric magma plumbing system of intraplate volcanoes as revealed by electrical resistivity image

Yabin Li¹, Aihua Weng¹, Wenliang Xu², Zonglin Zou^{1,3}, Yu Tang¹, Zikun Zhou¹, Shiwen Li¹, Yanhui Zhang^{1,4}, Guido Ventura^{5,6}

¹ *College of Geo-exploration Sciences and Technology, Jilin University, Changchun, China*

² *College of Earth Sciences, Jilin University, Changchun, China*

³ *China Petroleum Pipeline Engineering Corporation, Langfang, China*

⁴ *Shijiazhuang Tiedao University, Shijiazhuang, China*

⁵ *Istituto Nazionale di Geofisica e Vulcanologia, Roma, Italy*

⁶ *Istituto per lo studio degli impatti Antropici e Sostenibilità in ambiente marino, Capo Granitola (TP), Italy*

Supplemental Material

Materials and methods, supplementary figures

Materials and methods

Supplementary Figure S1

Supplementary Figure S2

Supplementary Figure S3

Supplementary Figure S4

Supplementary Figure S5

Supplementary Figure S6

Supplementary Figure S7

Supplementary Figure S8

Supplementary Figure S9

Supplementary Figure S10

Supplementary Figure S11

Supplementary References

Materials and methods

Magnetotelluric data. Our dataset included 9 long-period magnetotelluric (LMT) data and 31 broadband magnetotelluric (BBMT) data. LMT data were acquired in 2017 by LEMI-417 instruments with a record length >20 days. The PRC-MTMV software (Varentsov et al., 2003) was used to process the 2E+3H LMT data to obtain the full-impedance tensor of periods from 10 to 20,000 s. BBMT data were acquired mostly in 2018 by the instruments of PHOENIX GEOPHYSICS LIMITED, with a few dense data in the central area recorded in 2020. Acquisition time is >20 hr. BBMT signals (2E+2H) were converted to full-impedance tensor of periods from 3.25×10^{-3} to 2,000 s. Remote reference processing technique (Gamble et al., 1979) was utilized when heavy noises are present. The off-diagonal impedances at most stations are of good quality (**Fig. S1**). However, possible noise contamination, as well as the nature of the 1-D and 2-D at some stations and in certain period ranges can degrade the signal-to-noise ratio of the relatively small diagonal components (**Fig. S2**).

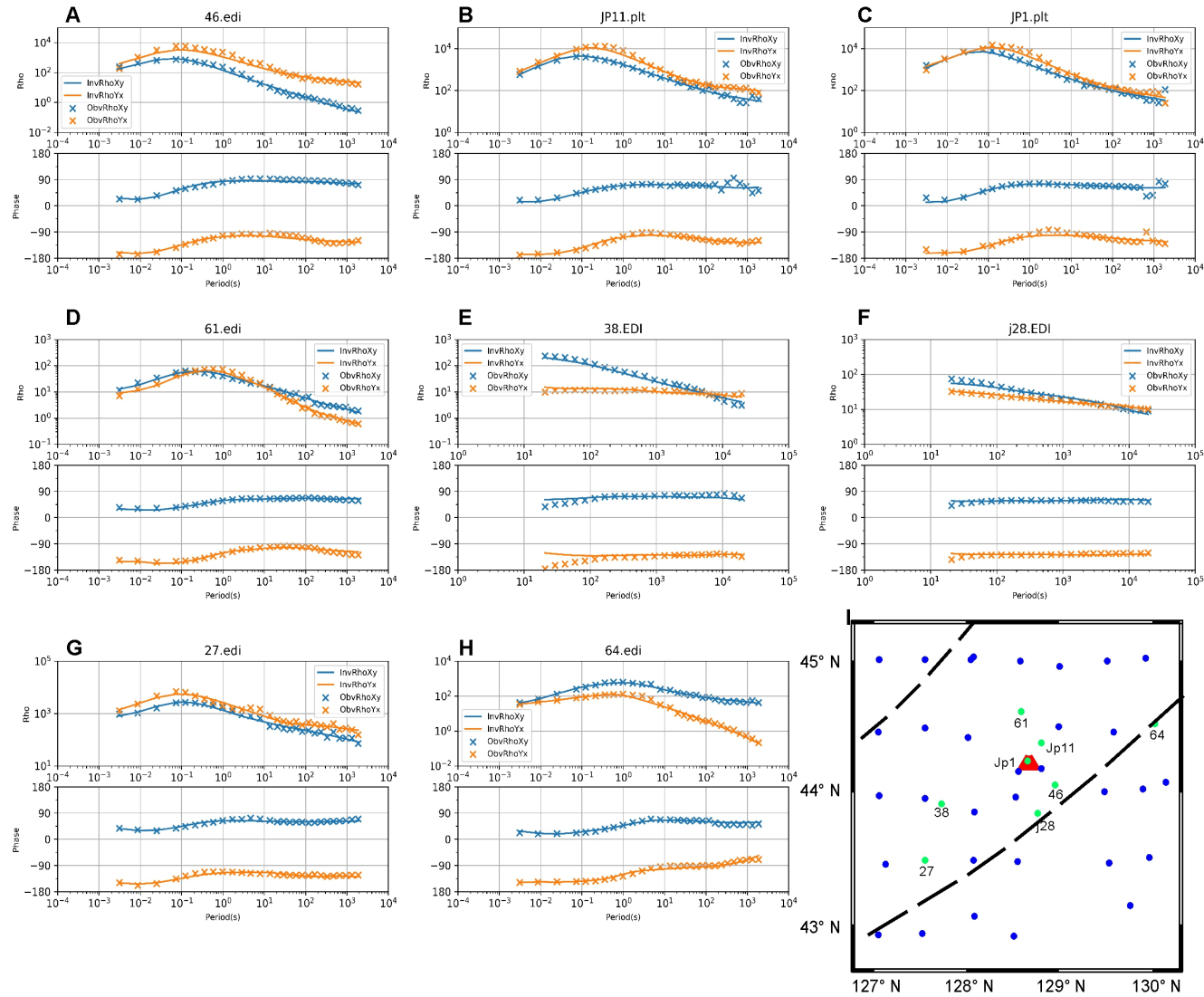
3-D modelling and inversion. We adopted the package ModEM (Egbert and Kelbert, 2012) to perform three-dimensional inversion. To obtain a good inversion, we run some tests before inversion including different model grid size, different initial model resistivity and different data types. These results are not shown in the Supplementary materials. Our preferred model was discretized with $40 \times 40 \times 45$ cells in the X (north - south), Y (east - west) and Z directions with 5 padding cells in horizontal and vertical directions, respectively. Horizontal grid has a dimension of 10 km by 10 km. 40 vertical layers are spaced logarithmically increasing by a factor of 1.16 from 100 m at the surface to 236 km. Horizontal and vertical smoothing factors are 0.3. The initial model was set to be a homogeneous half space with an initial resistivity of 100 Ω m. Inversion data have 37 periods from 0.00325 s to about 20,000 s. Error floors were set to $0.05 \times |Z_{xy} \cdot Z_{yx}|^{1/2}$ and $0.1 \times |Z_{xx} \cdot Z_{yy}|^{1/2}$ for the off-diagonal and diagonal components, respectively. All inversions started from an initial regularization parameter 10.0.

Compared to the full-impedance inversion, which terminated at a normalized misfit 3.19, the off-diagonal impedance inversion has a smaller normalized misfit of 2.24. The larger misfit in the full-impedance inversion is due to the noise in the diagonal impedance. The inversion models are shown in **Fig. S3**. We evaluated inversion quality by (a) cross-checking the predicted data with the observed ones (**Fig. S1**), (b) illustrating the spatial distribution and statistic histograms of nRMS (**Fig. S4**) and (c) comparing plane distribution of the apparent resistivity and impedance phase at four periods (**fig. S5**). All these comparisons indicate that the inversion converges at the stage where the model could reflect the characteristics of the observed data.

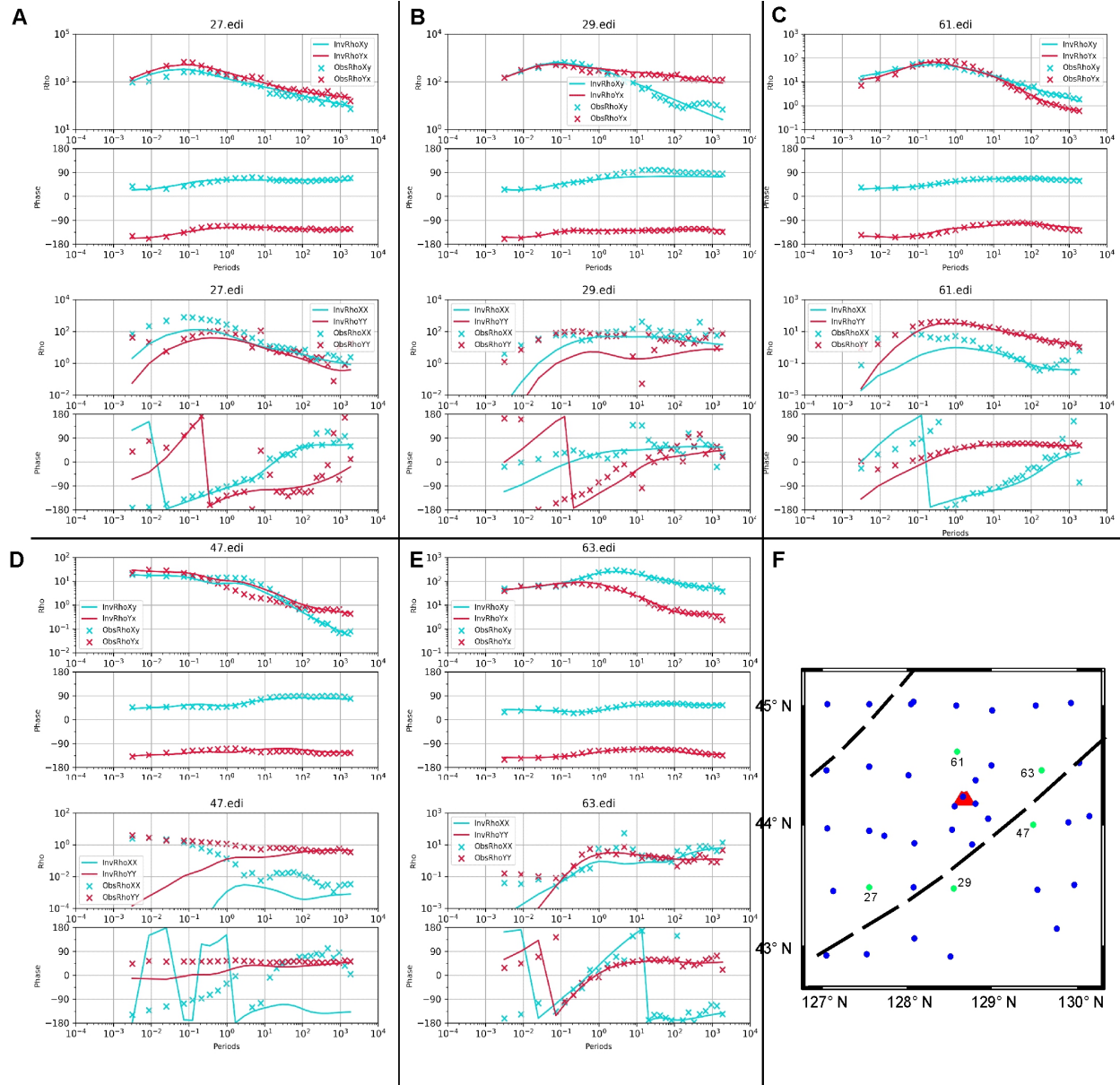
Sensitivity Tests. We verified the three low resistivity anomalies (c, d and e in **Fig. 2**) in the preferred model. The robustness of these anomalies can be reflected by the good data fits (**Fig. S5**). A few exceptions, e.g. site 75 at long periods, have bad fitting in their phase, possible due to noise.

We testify the obtained anomaly structure by synthetic data inversion (**Fig. S6**). The data are composed by off-diagonal impedance. The pathway from the asthenosphere through the lithosphere upward into the crust can be revealed rather well. Then, we tested the model dependency on the observed data using the method proposed by Robertson (2016). We compiled two datasets from the LMT data and the BBMT data, respectively. We inverted them using the same parameters as that of the preferred model inversion. Recovered models from the two data sets show an anomaly feature similar to that of the preferred model below the depth of 50 km (**Fig. S7**). LMT model at depth of 50 km is simpler than the models from the other two datasets suggesting that the large-site-spacing LMT cannot resolve the shallow anomalies. We finally confirmed the robustness of the anomalies c, d, e by applying a model perturbation method (Gribenko and Zhdanov, 2017). It is a forward modeling method that calculates the response of a new model whose anomalous resistivity is changed. Here, we define $RMS_{diff} = (RMS_{new} - RMS_{preferred}) / RMS_{preferred} \times 100\%$ to show the response change. RMS_{new} is the RMS of the new model, and $RMS_{preferred}$ denotes the RMS of the preferred inversion model. Changing the resistivity in these anomaly zone causes an

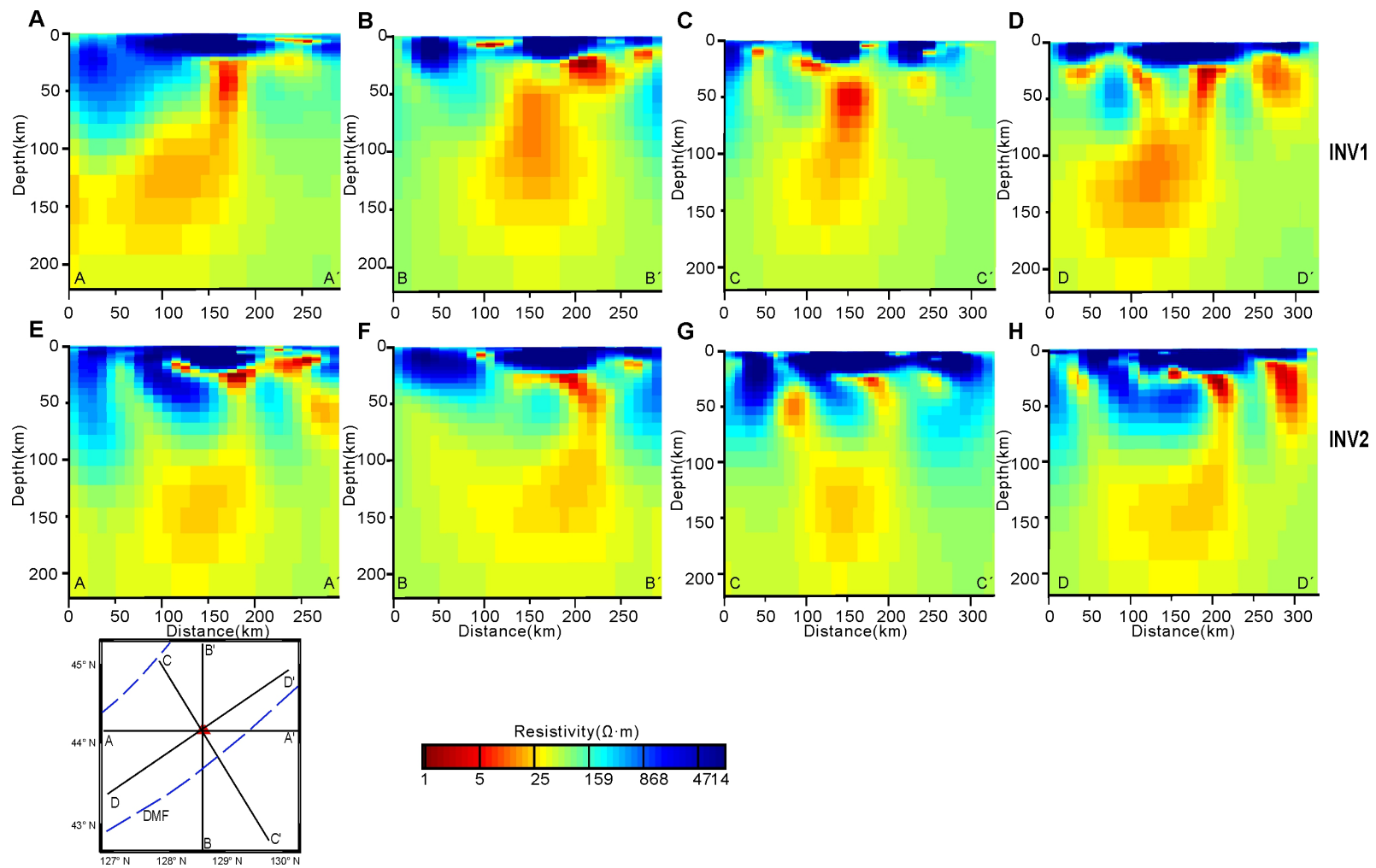
increase of RMS on the sites mainly above the anomalies, while the worse matchings distributed over more sites supports the existence of the magma pathway (see **Fig. S6**). It is worthwhile to note that when replacing anomaly e, the dramatic increase in RMS is mainly over the LMT sites. This implies that the LMT data mainly contribute to the detectability of anomaly e. Therefore, we conducted a further test on the reliability of this anomaly using the anomaly fixed inversion strategy (Burd et al., 2014). Here, we fixed the resistivity to be 100 Ω m at depths from 110 km to 180 km. This lock causes a significant increase in RMS and in the shape of the anomaly (**Fig. S9**).



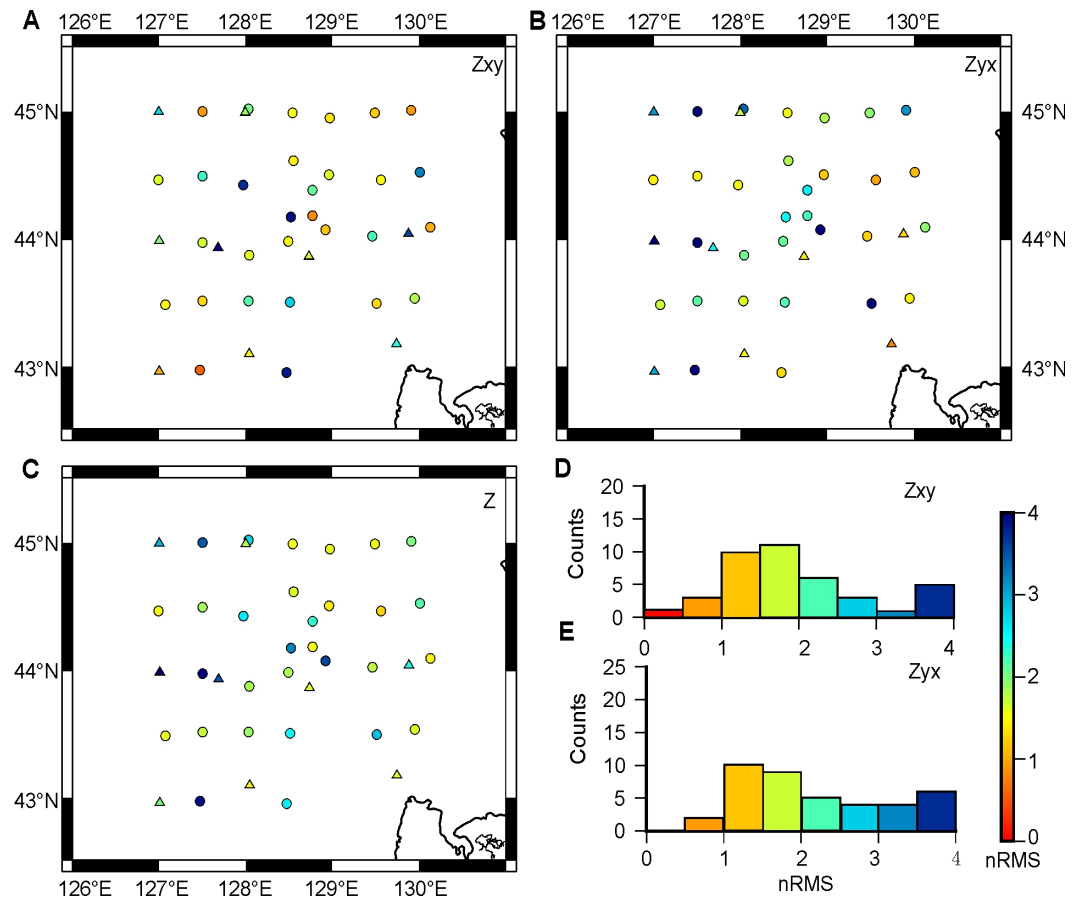
Supplementary Figure S1. Representative apparent resistivity and phase curves of off-diagonal impedance tensors around JMVf. Site 46, site JP1 and site JP11 are near JMVf. Sites 38 and 61 are located to the west and north of JMVf, respectively; site 64, sites j28 and 27 are near the Dunhua-Mishan Fault. Their locations are labeled in inset I.



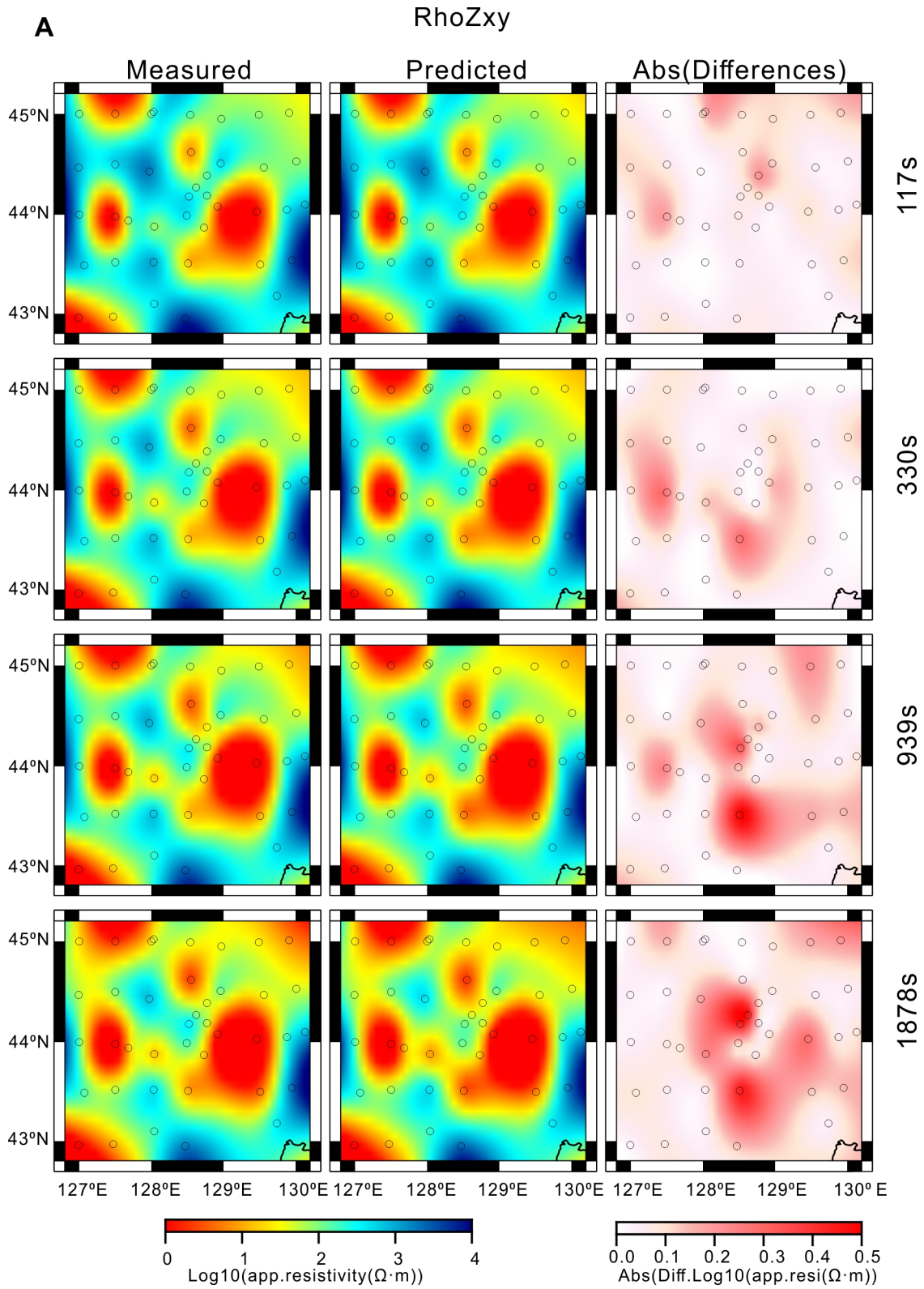
Supplementary Figure S2. Apparent resistivity and phase curves of full-impedance tensor at stations. Locations of the stations are labeled in **(F)**. Solid lines represent the theoretical response of the model from INV2 inversion.



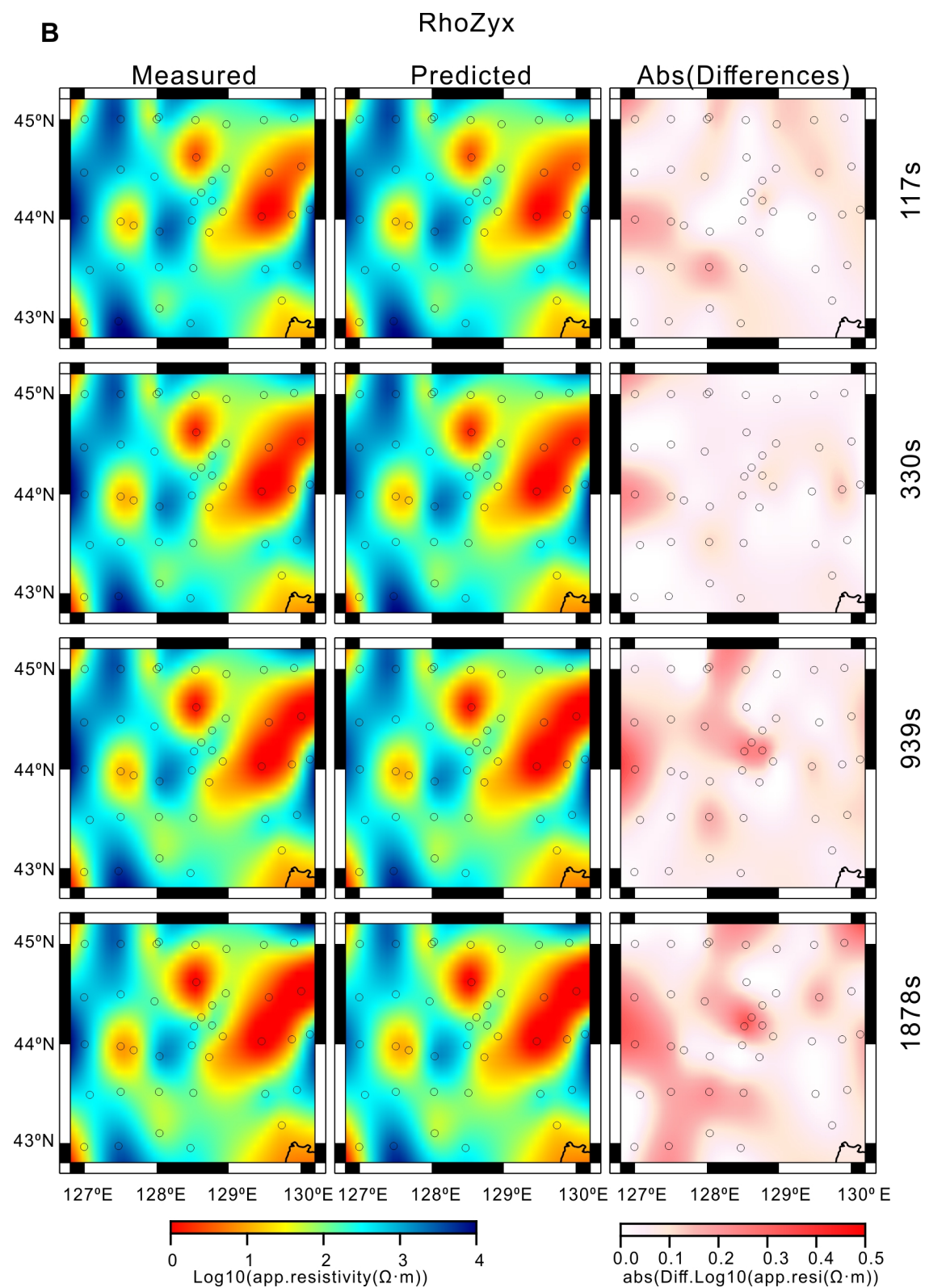
Supplementary Figure S3. Comparison of the inversion models from the off-diagonal components (Inv1) and the full-impedance tensor (Inv2). A–D: the resistivity sections along AA', BB', CC' and DD' in model Inv1. **E–H:** the resistivity sections along AA', BB', CC' and DD' in model Inv2.



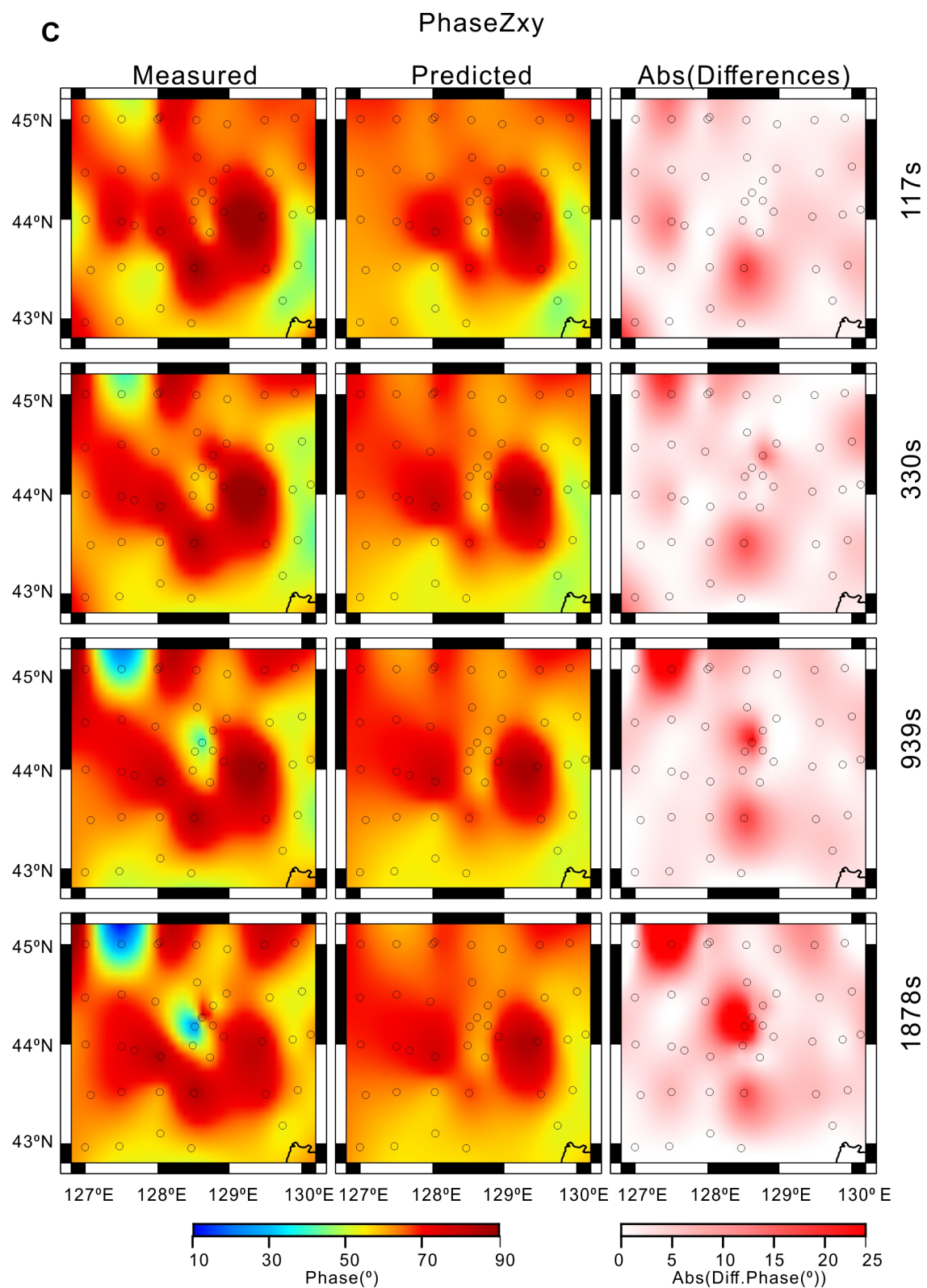
Supplementary Figure S4. Evaluation of the quality of the inversion from off-diagonal impedance tensor data. nRMS of Zxy component (**A**) and Zyx component (**B**) for each site. (**C**) nRMS for all Z components over each site. **D-E**: histograms of averaged nRMS for Zxy and Zyx, respectively. Triangles: LMT sites; circles: BBMT sites.



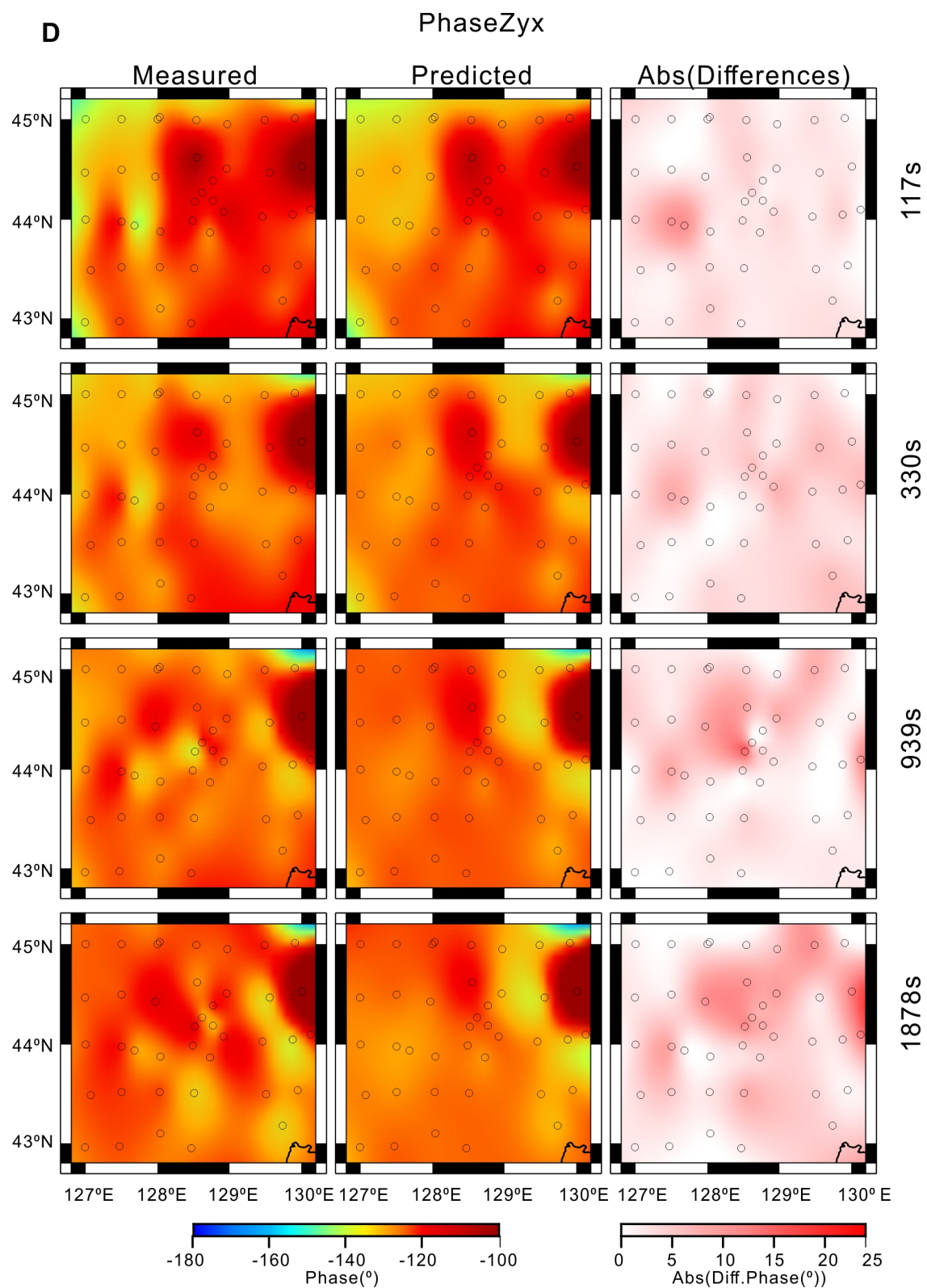
Supplementary Figure S5. Distribution of the observed and inverted impedance apparent resistivity and phase and their corresponding relative changes for different time periods. Columns from left to right are the observed data, the predicted data, and the absolute difference between the observed and predicted data. **A:** Comparison for rho-Zxy.



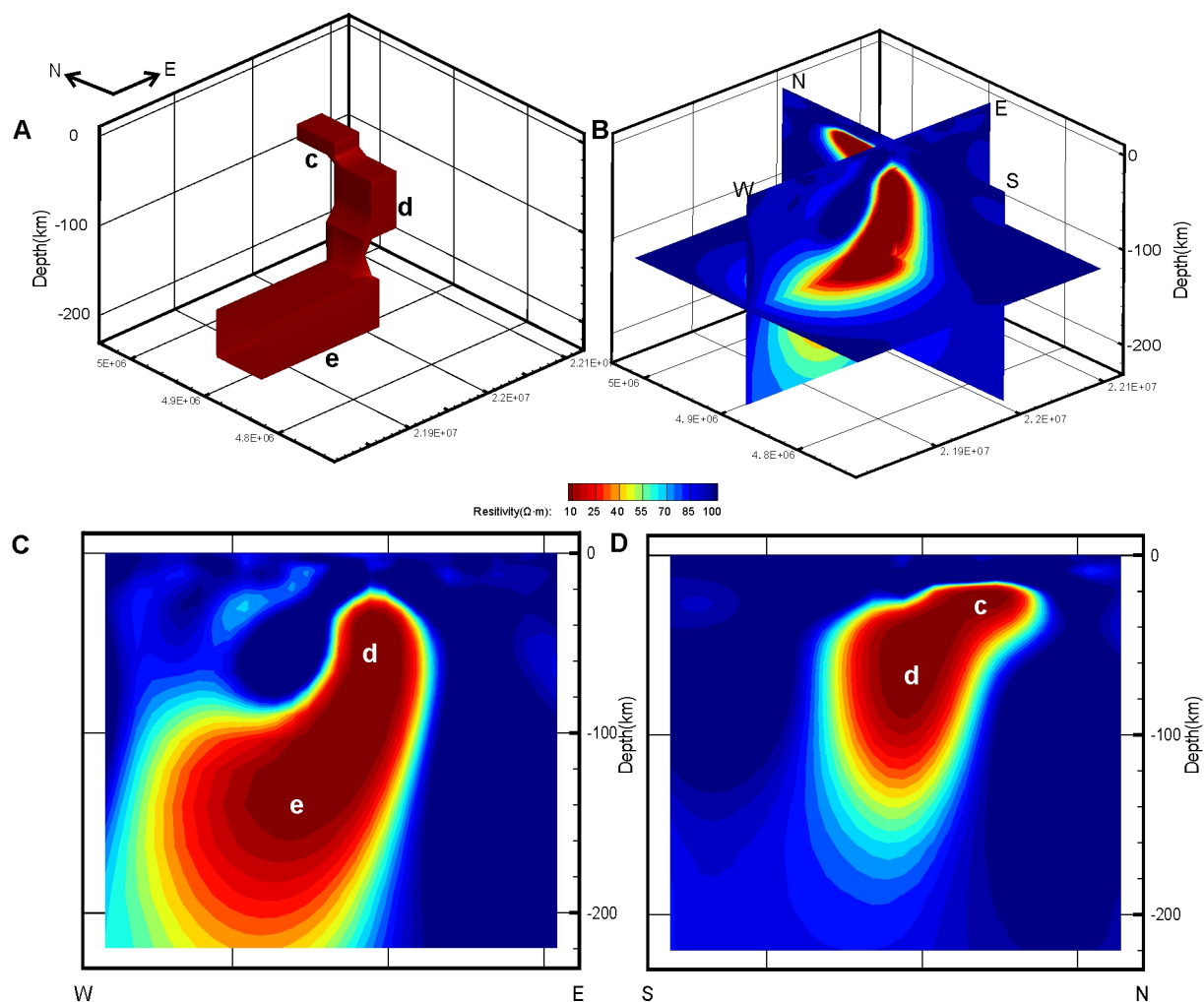
Supplementary Figure S5 (continued). B: Comparison for rho-yx component.



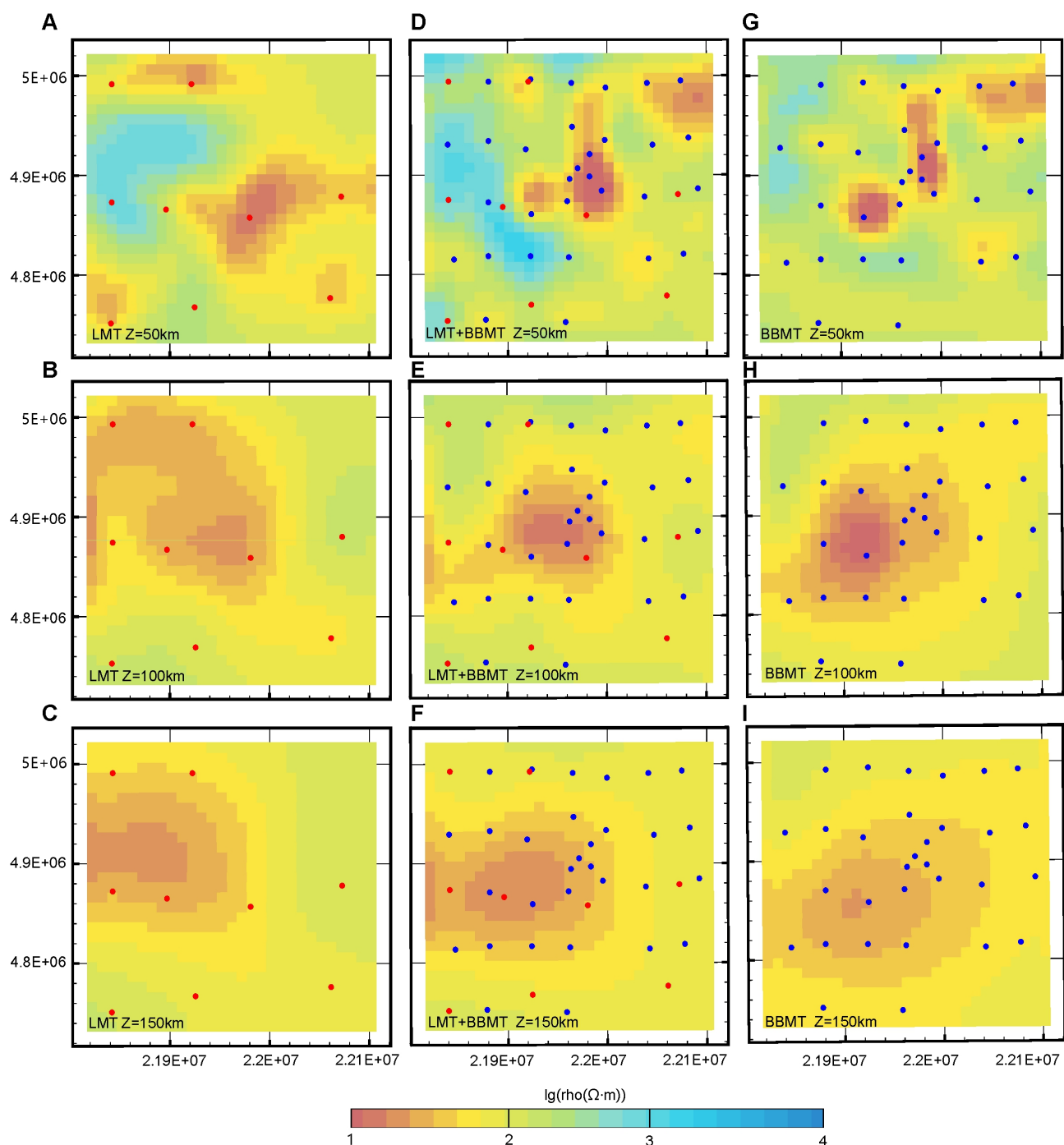
Supplementary Figure S5 (continued). C: Comparison of phase-Zxy component.



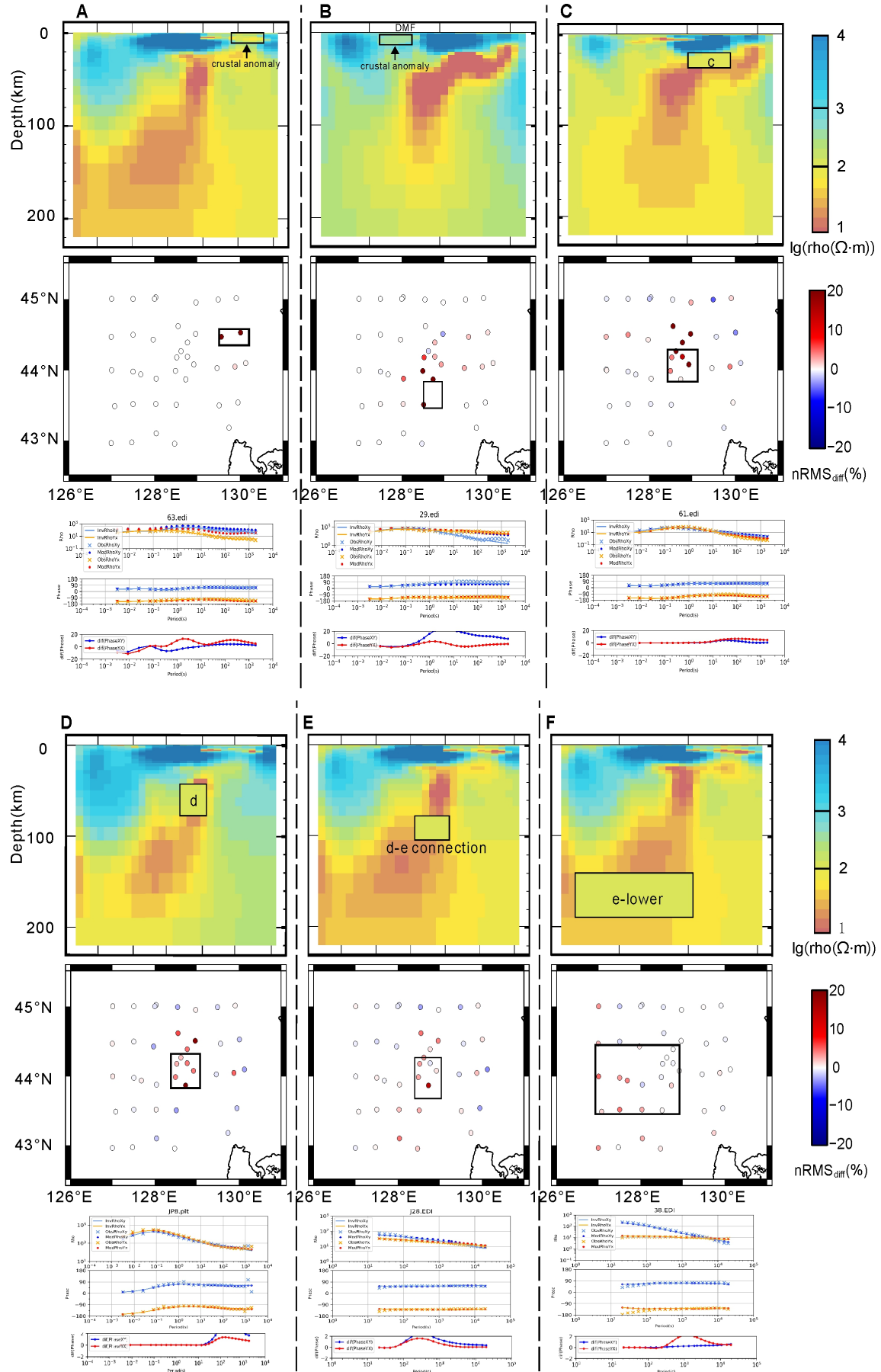
Supplementary Figure S5 (continued). D: Comparison of phase-Zyx component.



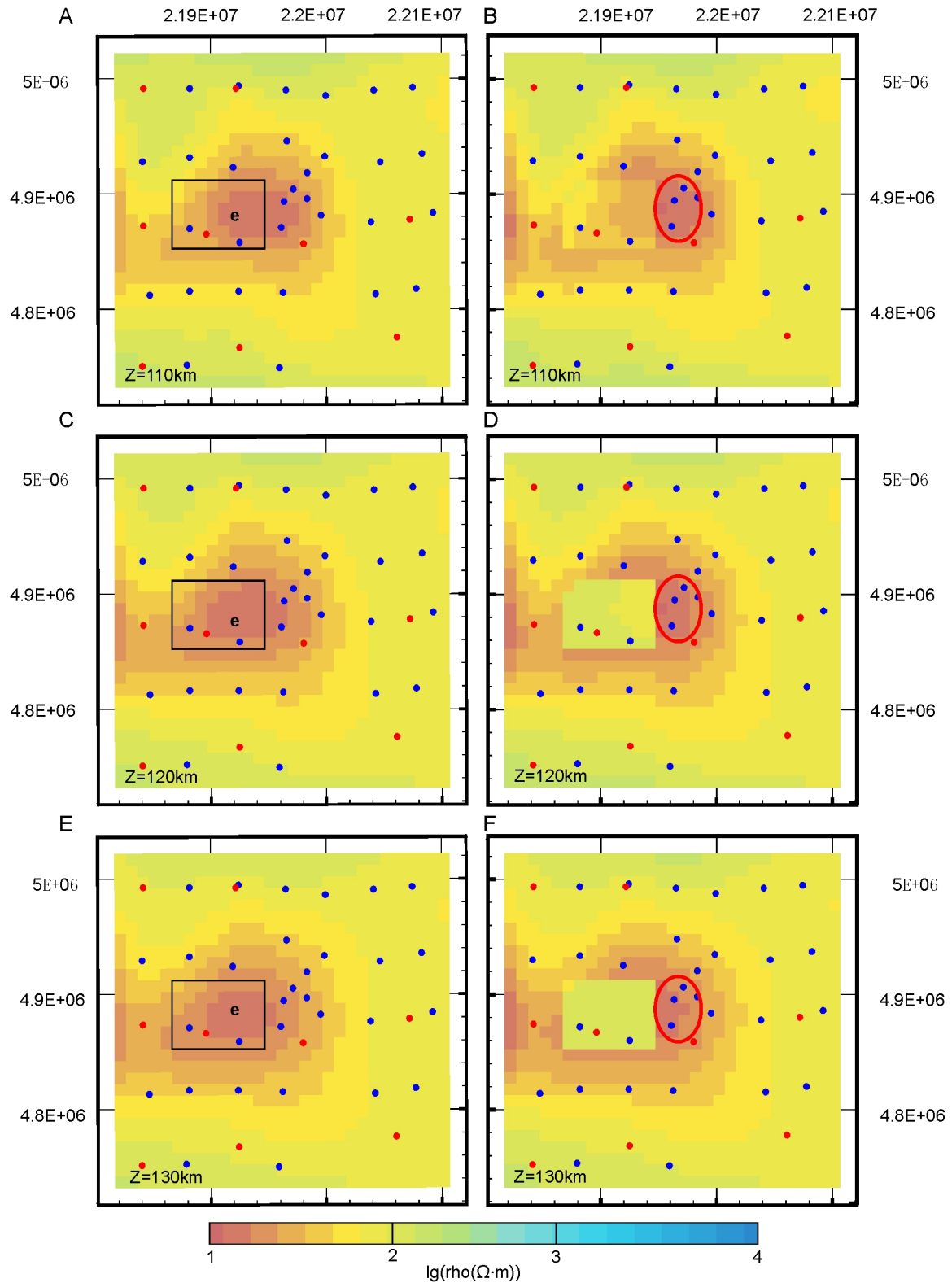
Supplementary Figure S6. Inversion Test for a 3D model mimicking our anomaly structure. A: Simplified model; **B-D:** the inversion model viewed by cross-sections.



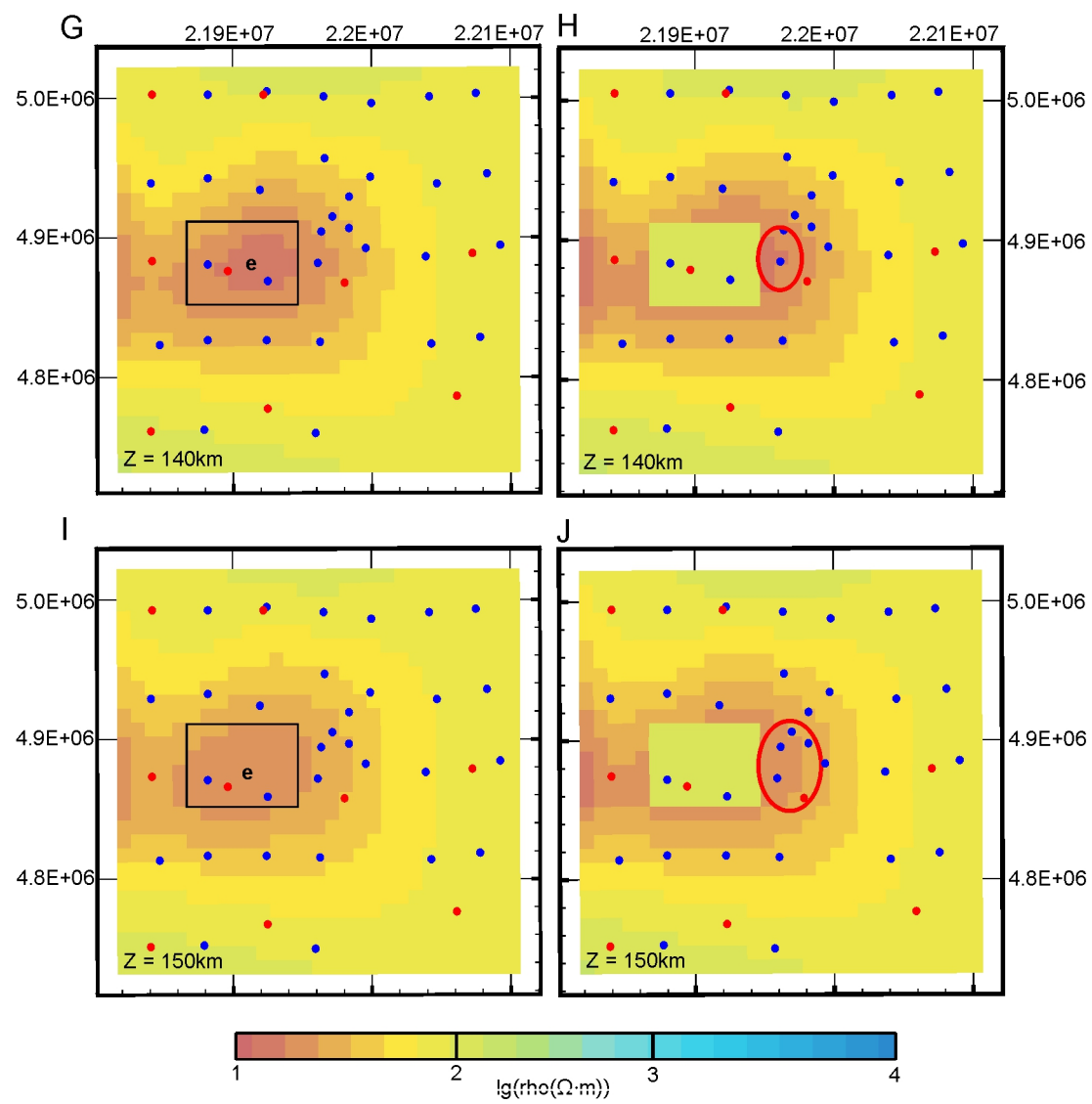
Supplementary Figure S7. Inversion results from different subsets of data. The columns from left to right are the horizontal slices of the models inverted from the data set of LMT (A, B, C), LMT+BBMT (D, E, F), and BBMT (G, H, I) observations. Top to bottom: slices at depth of 50, 100 and 150 km. Red dots: LMT sites; blue dots: BBMT sites.



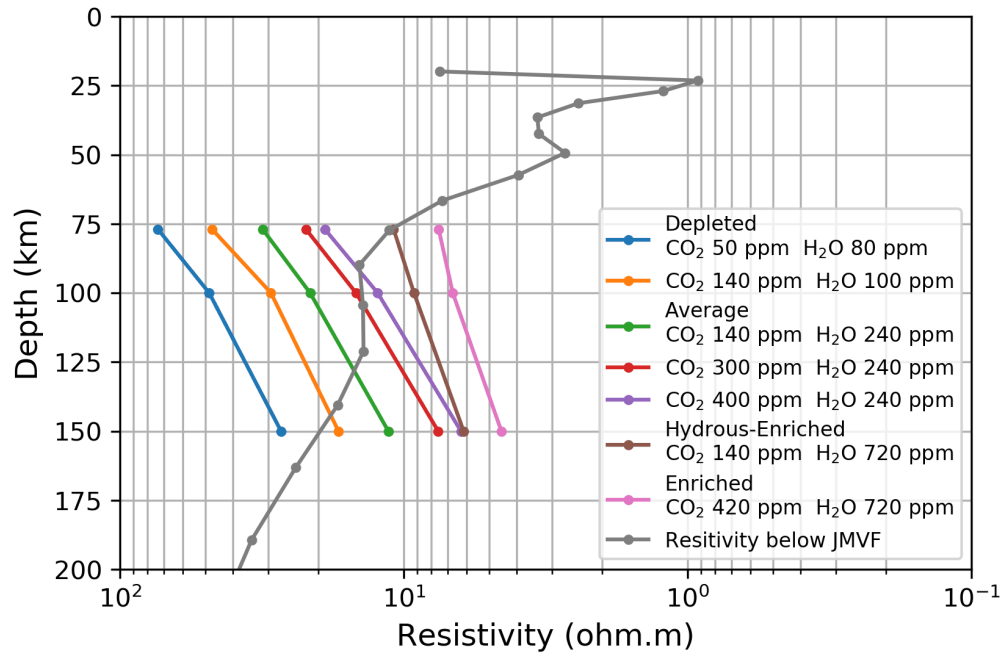
Supplementary Figure S8. Sensitivity analysis for anomalies at different depth. We testified 6 anomalies in (A) - (F). In each sub-graph, from top to bottom are shown the replaced model, the $nRMS_{diff}$ plane distribution and the responses curve fitting.



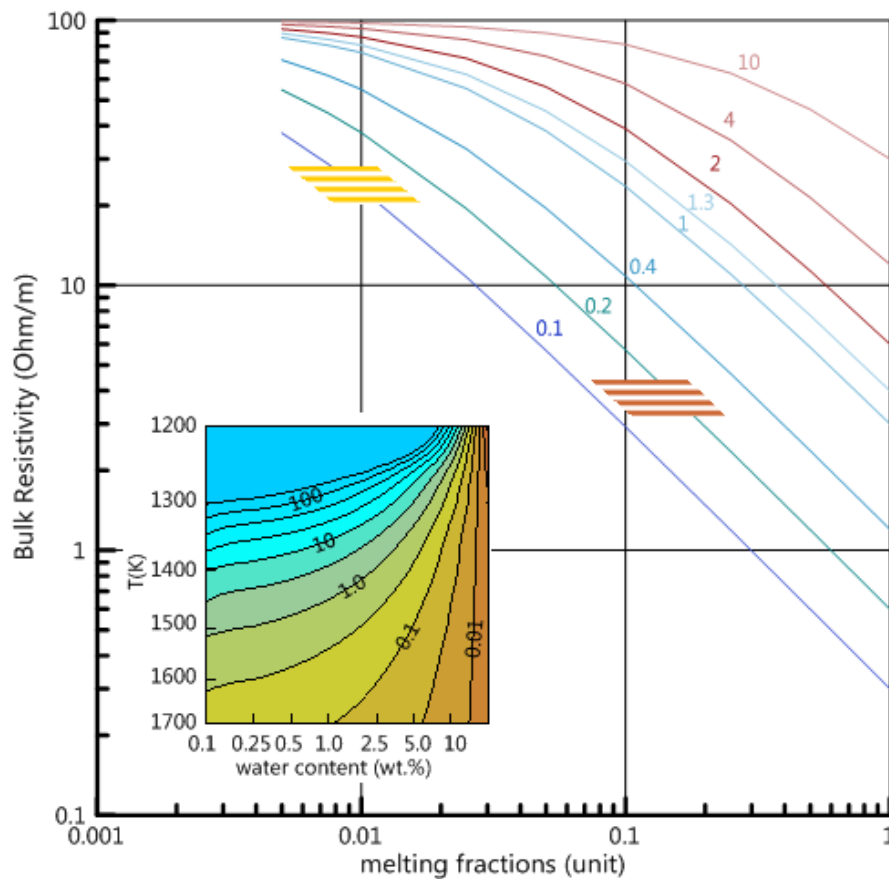
Supplementary Figure S9. Model obtained by the anomaly-fixed inversion. The rectangles in the left panel show the range where the resistivity is fixed to $100\ \Omega\cdot\text{m}$ for later inversion. Red circle: the anomalies out of the “fixed” area that are necessary to fit the observed data. Blue dots: BBMT sites; red dots: LMT sites.



Supplementary Figure S9 (continued).



Supplementary Figure S10. Bulk resistivity of mantle rocks (peridotite) as function of content of CO₂ and H₂O at selected P-T condition. The electrical resistivity model is from MAGLAB (Massuyeau et al., 2021). Here, we use the temperature profile from Fig. 3.



Supplementary Figure S11. Bulk resistivity of mantle rocks as function of melting fractions for a given melt resistivity. Anomaly d is the source of JMVf and its interpretation is hydrated peridotite partial melting. Here, we adapt the two-phase hybrid formula from Schmeling (1986). The melt resistivity (in $\Omega \text{ m}$) is numbered on the line of the same color. The resistivity of basaltic melts as function of water content and temperature (Ni et al., 2011) is shown by the inset. The yellow dashed zone represents the initial melting of anomaly d at the depth $\sim 75 \text{ km}$, where the temperature is estimated 1620 K (see Fig. 3). The melt may contain 1-2 wt.% H_2O using a value of 0.01 for the partition coefficient between melt and peridotite (Hirschmann et al., 2009). The melt has a resistivity of 0.1 to $0.13 \Omega \text{ m}$ (see the inset). The red-brown dashed zone gives the interpretation of the top of anomaly d, whose resistivity is about 4-6 $\Omega \text{ m}$ and the temperature is estimated to be about 1470 K (see Fig. 3). To interpret this anomaly, we estimated the possible melting fraction according to the Vs drop in the same zone (Flinders et al., 2018); the Vs drop is $\sim 3\%$, and we obtain a 4-6 vol.% melting fraction; by using this value as lower estimate of the melting fraction, the bulk resistivity is consistent with a melt resistivity of about $0.3 \Omega \text{ m}$. In referring to the inset of this figure, the H_2O content in the melt is $\sim 1\text{-}2 \text{ wt.}\%$. On the other side, if we take $\sim 2 \text{ wt.}\%$ H_2O , a value compatible with the geochemical observatories in other intraplate volcanoes in NE China, the resistivity of the melt is about $0.2 \Omega \text{ m}$ (see the inset). Therefore, a 7-15 vol.% melting fraction could reproduce the observed 4-6 $\Omega \text{ m}$ bulk resistivity.

Supplementary References

- Burd, A.I., Booker, J.R., Mackie, R., Favetto, A., and Pomposiello, M.C., 2014, Three-dimensional electrical conductivity in the mantle beneath the Payún Matrú Volcanic Field in the Andean backarc of Argentina near 36.5°S: Evidence for decapitation of a mantle plume by resurgent upper mantle shear during slab steepening: *Geophysical Journal International*, v. 198, p. 812–827, doi:10.1093/gji/ggu145.
- Egbert, G.D., and Kelbert, A., 2012, Computational recipes for electromagnetic inverse problems: *Geophysical Journal International*, v. 189, p. 251–267, doi:10.1111/j.1365-246X.2011.05347.x.
- Flinders, A.F., Shelly, D.R., Dawson, P.B., Hill, D.P., Tripoli, B., and Shen, Y., 2018, Seismic evidence for significant melt beneath the Long Valley Caldera, California, USA: *Geology*, v. 46, p. 799–802, doi:10.1130/G45094.1.
- Gamble, T.D., Goubau, W.M., and Clarke, J., 1979, Classic paper. Magnetotellurics with a remote magnetic reference.: *Geophysics*, v. 44, p. 53–68.
- Gribenko, A. V., and Zhdanov, M.S., 2017, 3-D Inversion of the MT EarthScope Data, Collected Over the East Central United States: *Geophysical Research Letters*, v. 44, p. 11,800–11,807, doi:10.1002/2017GL075000.
- Ni, H., Keppler, H., and Behrens, H., 2011, Electrical conductivity of hydrous basaltic melts: Implications for partial melting in the upper mantle: *Contributions to Mineralogy and Petrology*, v. 162, p. 637–650, doi:10.1007/s00410-011-0617-4.
- Robertson, K., Heinson, G., and Thiel, S., 2016, Lithospheric reworking at the Proterozoic–Phanerozoic transition of Australia imaged using AusLAMP Magnetotelluric data: *Earth and Planetary Science Letters*, v. 452, p. 27–35, doi:10.1016/j.epsl.2016.07.036.
- Schmeling, H., 1986, Numerical models on the influence of partial melt on elastic, anelastic and electrical properties of rocks. Part II: electrical conductivity: *Physics of the Earth and Planetary Interiors*, v. 43, p. 123–136, doi:10.1016/0031-9201(86)90080-4.
- Varentsov, I.M., Sokolova, E.Y., Martanus, E.R., and Nalivaiko, K. V., 2003, System of electromagnetic field transfer operators for the BEAR array of simultaneous soundings: Methods and results: *Izvestiya, Physics of the Solid Earth*, v. 39, p. 118–148.